The effect of mode II fatigue crack growth rate on the fractographic features of CFRP composite laminates

An acoustic emission and scanning electron microscopy analysis

Mohammadi, Reza; Najafabadi, Mehdi Ahmadi; Saghafi, Hamed; Saeedifar, Milad; Zarouchas, Dimitrios

DOI
10.1016/j.engfracmech.2020.107408

Publication date
2021

Document Version
Final published version

Published in
Engineering Fracture Mechanics

Engineering Fracture Mechanics 241 (2021) 107408

Contents lists available at ScienceDirect

Engineering Fracture Mechanics

journal homepage: www.elsevier.com/locate/engfracmech

The effect of mode II fatigue crack growth rate on the fractographic features of CFRP composite laminates: An acoustic emission and scanning electron microscopy analysis

Reza Mohammadi [a], Mehdi Ahmadi Najafabadi [a,*], Hamed Saghafi [b,c], Milad Saeedifar [d], Dimitrios Zarouchas [d]

[a] Non-destructive Testing Lab, Department of Mechanical Engineering, Amirkabir University of Technology, Tehran, Iran
[b] Department of Mechanical Engineering, Tafresh University, Tafresh, Iran
[c] New Technologies Research Center (NTRC), Amirkabir University of Technology, Tehran, Iran
[d] Structural Integrity & Composites Group, Faculty of Aerospace Engineering, Delft University of Technology, Delft, the Netherlands

ARTICLE INFO

Keywords:
Carbon/epoxy laminate
Fatigue damages features
Mode-II loading
SEM analysis
Acoustic emission

ABSTRACT

The present study is focused on the characterization of the fatigue damage features in carbon/epoxy laminates under mode-II loading conditions. To this aim, a sinusoidal cyclic load was applied to the End-Notched Flexural (ENF) specimens and the fatigue behavior of specimens was investigated. Scanning Electron Microscope (SEM) was used to identify the damage features on the fracture surface, i.e. fiber imprints, cusps, roller cusps, and striations. It was found that the fatigue damage features, such as cusps and striations, completely depended on the fatigue crack growth rate, *da/dN*. In addition, a linear relationship between the fatigue striation space and the strain energy release rate range (ΔGs) and the hysteresis loop area was established. The Acoustic Emission (AE) method was also employed to characterize the damage features. The obtained results showed that higher AE energy indicates larger and rougher cusps and striation features.

1. Introduction

Composite laminates have been widely applied in aerospace, marine, transportation, and other industries, because of their excellent mechanical properties and weight-saving potential. However, due to their low interfacial strength along the thickness direction, and the mismatch of the Poisson's ratios between the adjacent plies with different fiber orientations, delamination often occurs and it is one of the major damage modes found in these structures [1–5]. When this type of structure is subjected to fatigue loading, delamination can initiate and propagate due to the presence of manufacturing defects, free edge effect, external or internal ply drop, and impacts caused by foreign objects [6–10].

Generally, there are three modes of fracture: mode-I (opening mode), mode-II (sliding or in-plane shear mode) and mode-III (scissoring or out-of-plane shear mode). With a glance to open literature, the focus has been obviously more on mode-I fatigue behavior of composite laminates; and there is a lack of fundamental understanding of mode II fatigue delamination. This is especially due to the unstable crack growth behavior in mode II loading conditions which makes the crack growth study more difficult than mode I [11,12]. The unstable crack growth can dramatically decrease the fracture toughness because of the transition from a ductile fracture

* Corresponding author.
E-mail address: ahmadin@aut.ac.ir (M.A. Najafabadi).

https://doi.org/10.1016/j.engfracmech.2020.107408
Received 20 July 2020; Received in revised form 6 November 2020; Accepted 8 November 2020
Available online 12 November 2020

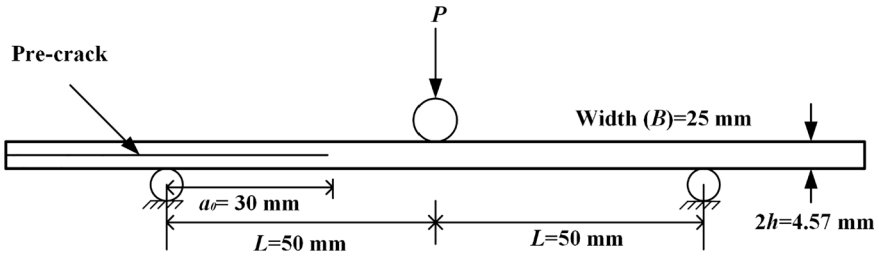

Fig. 1. The schematic of mode II test configurations.

mode in the case of a stable crack growth to a brittle fracture mode for an unstable growth [13].

The type of micro damage mechanisms occurred during the propagation of delamination in composite laminates generally depends on the loading, layup, manufacturing process, and adhesion quality between fiber and matrix [14–16]. It means that the fracture mode of a laminate can be determined according to the dominant damage mechanisms observed on its fracture surfaces. For example, the dominant feature in the mode-I fracture is the pulled-out fibers while shear cusps are common damage features for the quasi-static mode-II loading conditions [17]. The cusps are formed in mode II shear loading because of the stress state ahead of the crack tip. The shear stress ahead of the crack tip can be resolved into a principal stress, i.e. a tensile traction, which is inclined in an angle of 45° to the laminate plane. By increasing the load, angled cracks start to propagate in the 45° direction. When these angled cracks coalesce, the cusps patterns are formed [14,18,19].

For the mode II fatigue loading conditions, these cusps are infinitesimally deformed in each loading cycle because of the relative slippage of the upper and lower surfaces of the delamination. After a considerable number of cycles, these infinitesimal deformations are accumulated and form the matrix rollers [20]. Amaral et al. [21] defined a process zone, ahead of the crack front, including cusps and other damage features. They proposed that an effective crack length containing the process zone should be defined instead of the real crack tip and the energy dissipated in the process zone should be also considered while assessing the fatigue delamination.

Striation is another fracture feature, which can be observed ahead of the crack tip during fatigue loading [22,23]. Striations generally appear as regular ripples or marks on the fracture surfaces. Striations are formed on the fiber imprints because of the decohesion of fiber and resin at high-stress ratios [21,24]. A practical use of this feature is to determine the delamination growth rate by both measuring the distance between these striations and considering the load cycle frequency [15]. The process for striation formation entails the molecular chains being fractured at the crack tip ('chain scission') following limited stretching [14]. This feature appears as a series of bright or dark lines or grooves within the imprints orientated perpendicular to the fiber direction. Detailed observations of the striations have indicated that they may be formed due to the extension of micro-cracks at the fiber–matrix interface [14,25,26]. Limited studies [20,24,27] have been conducted on the variation of cusps and striations during crack propagation under fatigue loading. Khan et al. [27,28] investigated the delamination growth under mode I fatigue loading in carbon/epoxy laminates. The results showed that the striation space increases when either the load range or the maximum load increases.

Nowadays, Structural Health Monitoring (SHM) techniques are frequently used for monitoring the damage of composite laminates. Acoustic Emission (AE) is one of the most popular SHM techniques that has been widely used for detecting, analyzing and clustering of the damage mechanisms in composite materials [29–31]. AE is defined as the generation and propagation of a transient elastic wave caused by a sudden release of strain energy which can be due to damage occurrence in the material [32–34]. The literature review revealed that this technique has been mainly used to consider the damage behavior of composite laminates under quasi-static loading [32,35–37] while in just limited studies it has been used for the fatigue loading conditions [21,38–40]. In the present study, Scanning Electron Microscope (SEM) images and AE technique have been used to investigate the effect of mode II fatigue crack growth rate, da/dN, on the fatigue micro-damage features, i.e. fiber imprint, cusps, roller cusps, and striations.

Based on the best authors' knowledge, no systematic study has been conducted on the effect of fatigue delamination growth rate on the fractographic features of CFRP composites, therefore, the present study aims to quantitatively investigate this subject by means of SEM and AE techniques.

2. Experimental procedures

2.1. Materials and specimens

The test specimens were made of AS4/8552 carbon/epoxy prepreg, supplied by Hexcel Company, USA. Twenty four prepreg plies were laminated to produce the specimens. A 12.7 μm-thick Fluorinated Ethylene Propylene (FEP) film was inserted between the 12th and 13th plies (mid-thickness of the laminate) to create the initial pre-crack. The curing process was performed according to the datasheet provided by the manufacturer [41]. After the curing process, all specimens were cut out of the panel using a horizontal milling machine equipped by a very sharp rotary cutting disk with a precision of 1 μm. In order to reduce the manufacturing variations, all the fatigue and quasi–static specimens were cut out of the same composite panel. The specimens were cut to 180 mm in length and 25 mm in width. The End-Notched Flexural (ENF) fixture was used to perform the mode-II tests. Fig. 1 shows the geometry of the specimens and the mode II test setup. Finally, the prepared specimens were tested under mode-II loading conditions according to ASTM D7905M standard [42].

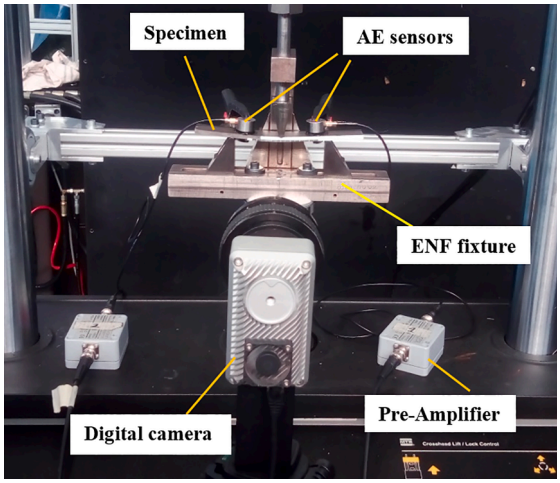

Fig. 2. The testing machine and the mode II experimental test setup for the quasi-static and fatigue loading conditions.

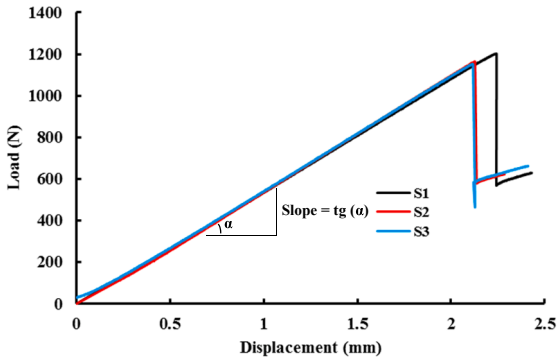

Fig. 3. Load-displacement curves for the specimens subjected to the quasi-static mode-II loading.

2.2. The testing machine

All quasi-static and fatigue tests were performed using a 10 kN universal hydraulic tensile-compression machine, MTS-810. Fig. 2 illustrates the testing machine and the utilized test apparatus, i.e. the digital camera, AE sensors, preamplifiers, and the fixture. The digital camera has a 4 MP resolution with a frame rate of 55 fps, supplied by OPTOMOTIVE Company. The crack length was monitored during the quasi-static tests by taking one image per second using the digital camera. While, during the fatigue test, after each 500 cycles, the specimen was hold at the maximum load for a few seconds to let the digital camera to take an image.

2.3. Acoustic emission device

The AE activity, during the quasi-static and fatigue tests, was recorded using two AE sensors placed on the specimen surface, as depicted in Fig. 2. The AE sensors were broadband, single-crystal, and resonant type, VS900M, supplied by Vallen Systeme GmbH. The frequency range of the sensors is [100–900 kHz]. Two pre-amplifiers with a gain of 34 dB were used for amplifying the recorded signals. The threshold of the receiving AE events and the sampling rate were 50 dB and 2 MHz, respectively. An appropriate coupling was achieved by applying the ultrasonic gel at the interface of the AE sensors and the specimen surface. The reproducibility of the AE sensors was checked before each test by conducting the standard pencil lead breakage test [43].

3. Results and discussion

3.1. The quasi-static test

The mode II quasi-static tests were first conducted to obtain the required inputs for performing the mode II fatigue tests. Nine specimens were totally tested under the quasi-static and fatigue loading conditions, which are called S1 to S9 hereafter. The first three specimens, i.e. S1 to S3, were tested under the quasi-static loading conditions to obtain the interlaminar fracture toughness and the

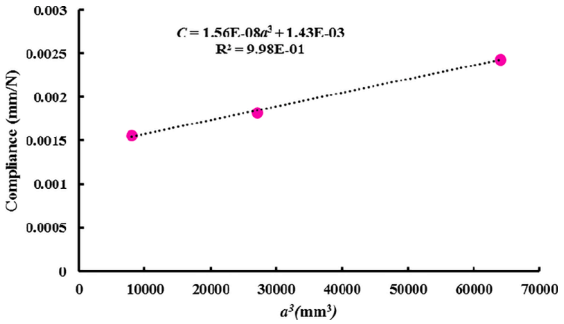

Fig. 4. Compliance vs cube of delamination length for specimen S1.

Table 1
Calculation of CC parameters and G_{IIC} values for the quasi-static tests.

Specimen	K (N/mm) At a_0 = 30 mm	A (mm/N)	m (1/N·mm^2)	δ_{max} (mm)	P_{cr} (N)	G_{IIC} (kJ/m^2)
S1	546	1.43E−03	1.56E−08	2.24	1202.63	1.21
S2	562	1.44E−03	1.45E−08	2.12	1165.26	1.05
S3	559	1.45E−03	1.46E−08	2.10	1153.06	1.04
Average	555.6 ± 8.5	1.45E−03 ± 1E−5	1.46E−08 ± 6.08E−10	2.12 ± 0.07	1173.63 ± 25.82	1.10 ± 0.09

critical load and displacement values which were vv then used to set the fatigue test parameters. The six remained specimens, i.e. S4 to S9, were tested under the fatigue loading conditions. The quasi-static tests were conducted according to ASTM D7905M standard [42]. The quasi-static specimens were loaded under displacement-control mode with a constant crosshead rate of 0.5 mm/min. The load and displacement were continuously recorded by the machine. Fig. 3 presents the load–displacement curve of the quasi-static specimens. According to this figure, the slope of the initial linear elastic part of the curves (K) for all specimens is almost the same. The average values of the maximum load and its corresponding displacement are 1173.63 N and 2.15 mm, respectively.

Mode II interlaminar fracture toughness (G_{IIC}) is calculated as follows (recommend by ASTM D7905M) [42]:

$$G_{IIC} = \frac{3mP_{cr}^2 a_0^2}{2B} \tag{1}$$

where B is the specimen width (25 mm), P_{cr} is the maximum load of the load–displacement curve, a_0 is the initial crack length (30 mm), and m is the compliance calibration (CC) coefficient obtained from CC tests. The ratio of the displacement to the load (δ/P) is defined as the compliance value. According to the standard procedure [42], the CC coefficient is obtained by conducting two preliminary tests with the crack length of 20 and 40 mm, before starting the main fracture test with a crack length of 30 mm. The preliminary tests shall not lead to the crack propagation in the specimen. Therefore, the compliance tests were stopped when the load reached 500 N (<50% of the maximum load). Therefore, the compliance is calculated based on the initial linear elastic part of the load–displacement curve.

Finally, obtained compliance values are plotted against the a^3 and a line is fitted to the data as depicted in Fig. 4. The parameters of A and m are obtained from the fitted linear equation as follows:

$$C = A + ma^3 \tag{2}$$

where a is the crack length, m and A are the CC coefficients, and C is the compliance. According to Fig. 4, the average values of m and A for the quasi-static tests are 1.46E−8 1/N·mm^2 and 1.45E−3 mm/N, respectively. Table. 1 presents the obtained results from the quasi-static tests. The G_{IIC} values for specimens S1, S2, and S3 are 1.21, 1.05, and 1.04 kJ/m^2, respectively. The average values of G_{IIC} and P_{cr} were used to calculate the input parameters of the fatigue tests.

3.2. The fatigue tests

The preliminary CC tests were carried out before each fatigue test and CC parameters (A, m) were calculated. The same 3-point bending fixture (see Fig. 2) was used for the fatigue tests. All fatigue tests were conducted under load-control conditions with a constant loading ratio ($R = P_{min}/P_{max}$) of 0.3. The load-control mode was selected because it guarantees a large enough delamination growth and leads to an increasing crack growth rate by proceeding the fatigue test. The sinusoidal cyclic load with a frequency of 3 Hz was applied to the specimen because higher frequencies resulted in the specimen slippage during the fatigue test which is undesirable. In addition, higher frequencies can lead to the heat generation in the specimen, which is more critical for matrix and fiber /matrix interface because the high temperature can soften matrix [44–47]. The fatigue tests were conducted at different ratios of G_{IImax}/G_{IIC} (0.4, 0.5, and 0.6). The ratio did not go higher than 0.6 because in the case of higher ratios, the crack growth became unstable.

Table 2
The fatigue tests characteristics.

Specimen	A (mm/N)	m (1/N·mm^2)	G_{IIimax}/G_{IIC}	P_{max} (N)	P_{min} (N)
S4	0.00140	1.45E−08	0.4	677	203
S5	0.00141	1.60E−08	0.4	677	203
S6	0.00137	1.44E−08	0.5	757	227
S7	0.00138	1.43E−08	0.5	757	227
S8	0.00142	1.42E−08	0.6	829	249
S9	0.00142	1.49E−08	0.6	829	249

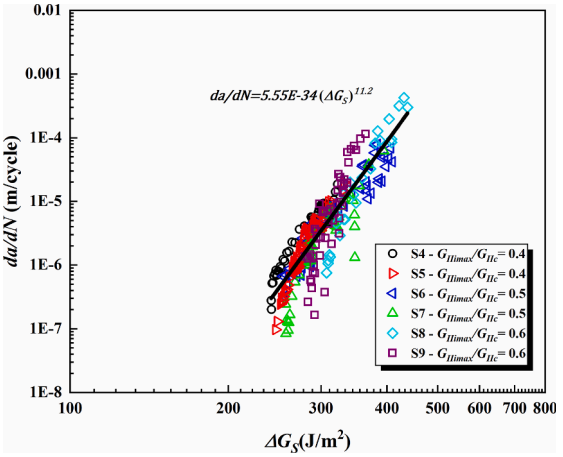

Fig. 5. da/dN vs ΔG_s graph for all fatigue specimens.

According to these ratios, P_{max} and P_{min} were obtained using Eqs. (3) and (4):

$$\frac{G_{IIimax}}{G_{IIC}} = \left(\frac{P_{max}}{p_{cr}}\right)^2 \tag{3}$$

$$R = P_{min}/P_{max} = 0.3 \tag{4}$$

where G_{IIC} is mode II fracture toughness (1.10 kJ/m^2), G_{IIimax} is the maximum energy release rate at the first fatigue loading cycle, and P_{cr} is the average of maximum force obtained from the quasi-static tests, as reported in Table 1 (1173.63 N). The fatigue output data such as the number of cycles (N), the maximum load (P_{max}), the minimum load (P_{min}), the maximum displacement (δ_{max}), and the minimum displacement (δ_{min}) were recorded at each cycle by the machine. During the fatigue tests, the specimens were subjected to the cyclic load until the crack tip reached under the loading roller (see Fig. 1). Because of the high compression force presented under the loading roller, the crack could not propagate furthermore. Table 2 presents the fatigue test characteristics.

According to the standard [42], the instantaneous crack length (a) at each cycle during the fatigue test can be obtained by Eq. (5):

$$a_i = \left(\frac{C_i - A}{m}\right)^{\frac{1}{3}} \tag{5}$$

where A and m are CC parameters obtained from the preliminary CC tests, and a_i and C_i are the crack length and the compliance corresponding to cycle N_i, respectively. C_i is calculated as follows [42]:

$$C_i = \frac{(\delta_{max})_i}{P_{max}} \tag{6}$$

where P_{max} is the maximum load and $(\delta_{max})_i$is the maximum displacement at i^{th} cycle. The crack growth rate, da/dN, is then calculated as follows [48]:

$$\left(\frac{da}{dN}\right)_i = \frac{a_{i+1} - a_i}{N_{i+1} - N_i} \tag{7}$$

where a_i is the crack length corresponding to the cycle number N_i, and a_{i+1} and N_{i+1} are the crack length and the cycle number corresponding to the next available data point. The strain energy release rate range (ΔG_s) in the current cycle is calculated using Eqs. (8)–(10) [49]:

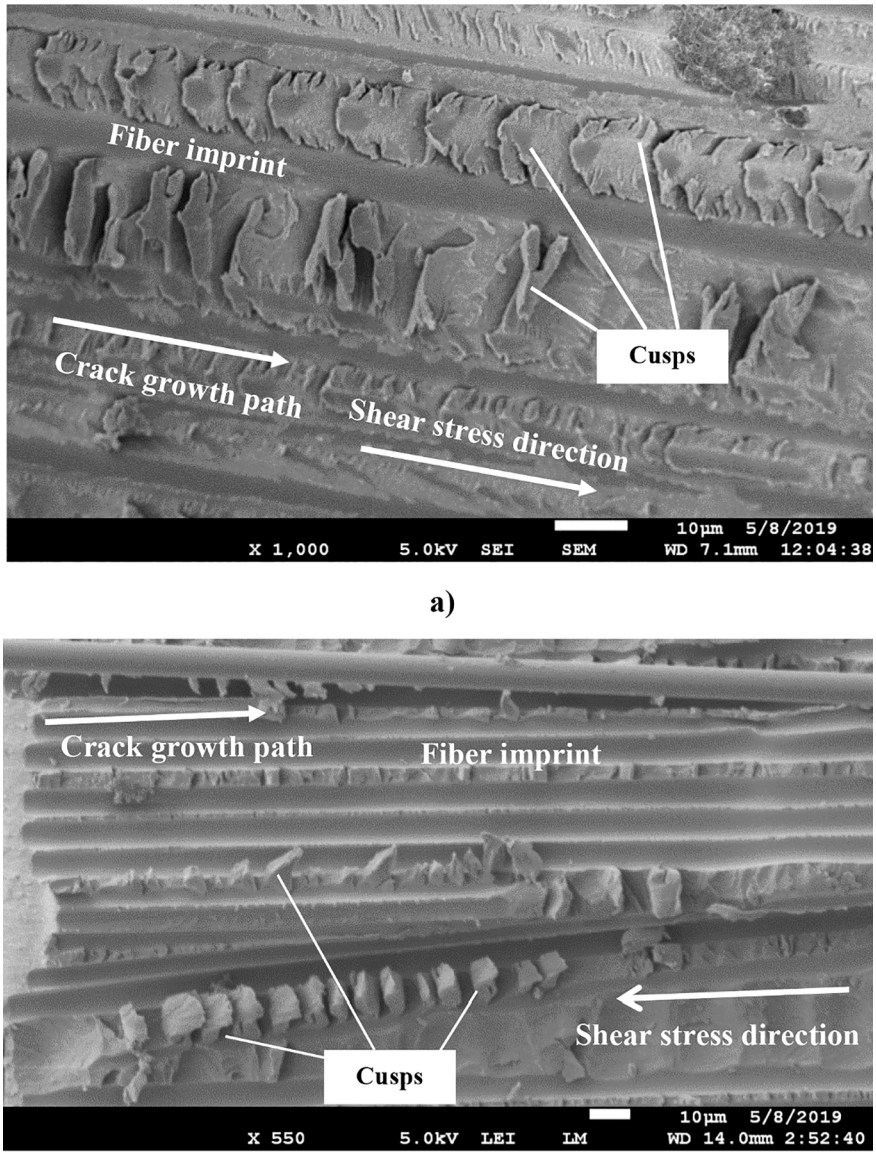

Fig. 6. The fracture surface of the quasi–static mode II test specimen; (a) the upper surface, and (b) the lower surface.

$$(G_{II\max})_i = \frac{3m}{2B}(P_{\max}a_i)^2 \tag{8}$$

$$(G_{II\min})_i = \frac{3m}{2B}(P_{\min}a_i)^2 \tag{9}$$

$$\Delta G_s = \left(\sqrt{G_{II\max}} - \sqrt{G_{II\min}}\right)^2 \tag{10}$$

Fig. 5 shows the crack growth rate vs ΔG_s for all fatigue specimens. As seen, the crack growth rate increases by enhancing ΔGs values and the different values of G_{IIimax}/G_{IIC} do not have a significant effect on the fatigue crack growth behavior.

3.3. Fractography analysis

The SEM images was used to investigate the fracture surface of the specimens after the quasi-static and fatigue tests. The most relevant fractographic features in mode II loading conditions are cusps, appeared on the damaged surface as raised platelets

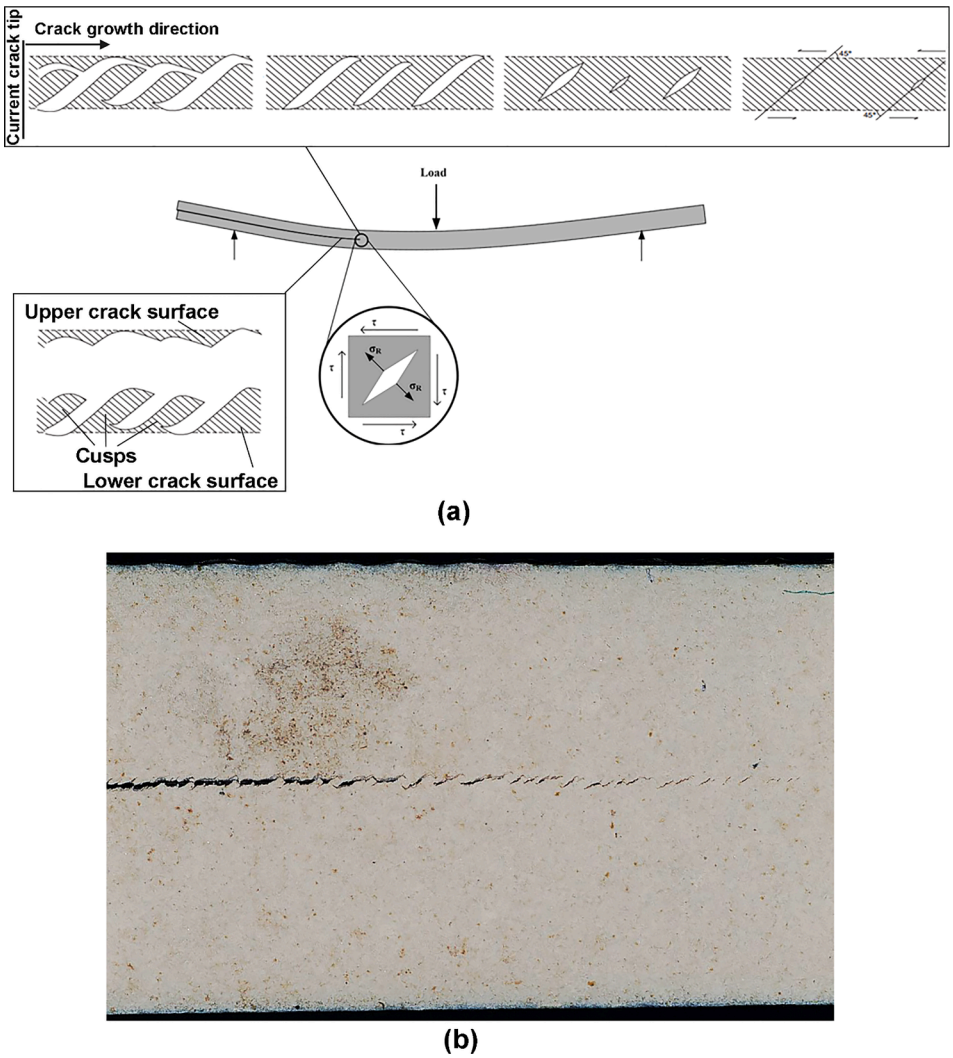

Fig. 7. The formation of cusps during the mode II loading conditions; (a) a schematic view, and (b) a real image from the side of the ENF specimen.

[14,26,50]. Fig. 6 illustrates the fracture surface of one of the quasi-static specimens. The dominant fracture features, which are obviously visible in Fig. 6, are fiber imprint and matrix failure in the form of cusps. The direction of the global crack growth can be deduced using the cusp's orientation because the tilt of cusps is formed opposite to the shear stress direction. In mode II loading conditions, the shear stress direction on the upper surface is in the same direction of the crack growth (Fig. 6a) while on the lower surface, it is opposite to the crack growth direction (Fig. 6b). Therefore, the cusps on the lower surface are oriented along the crack growth direction while the cusps on the upper surface are formed opposite to the crack growth direction. A schematic for the cusps formation process under mode II loading conditions is shown in Fig. 7. As shown, because of the stress state at the crack tip, the angled matrix cracks initiates. By increasing the load, these cracks are enlarged and connected together to create cusps.

Fig. 8 depicts the fracture surface of the specimen subjected to the fatigue loading. In order to study the effect of the crack growth rate on the damage features, SEM images were taken from the fracture surface at different distances (Δa) from the initial crack tip. By knowing the actual crack length ($a_0 + \Delta a$) at each point, the crack growth rate (da/dN) can be calculated using Eq. (7). As seen in Fig. 8a, taken from 1 mm ahead of the initial crack tip (the corresponding crack growth rate of 2E−7 m/cycle), the fracture surface and the fiber imprints are almost clean. Fig. 8b shows the fatigue surface when the crack growth rate was $da/dN = 3E{-}6$ m/cycle. In this case, the cusps are deteriorated because of the slippage of the upper and lower crack surfaces in mode II cyclic loading. By comparing Fig. 8c&d and a&b, it is obvious that by increasing the crack growth rate, the damage features are expanded and enlarged. In the case of fiber imprint patterns, they are not clear and continuous at the high crack growth rates anymore (see Fig. 8c&d). As reported in the literatures [9,51], by increasing the loading rate and consequently the delamination growth rate, less fiber/matrix interface failure and more matrix brittle cracking are observed on the fracture surface. However, in the present study, because the maximum delamination growth rate in the fatigue tests, 6E–5 m/cycle, is not really high, it is not expected that the damage mechanism completely changes from debonding to matrix cracking while the fatigue delamination growth rate increases from 2E–7 m/cycle to 6E–5 m/cycle.

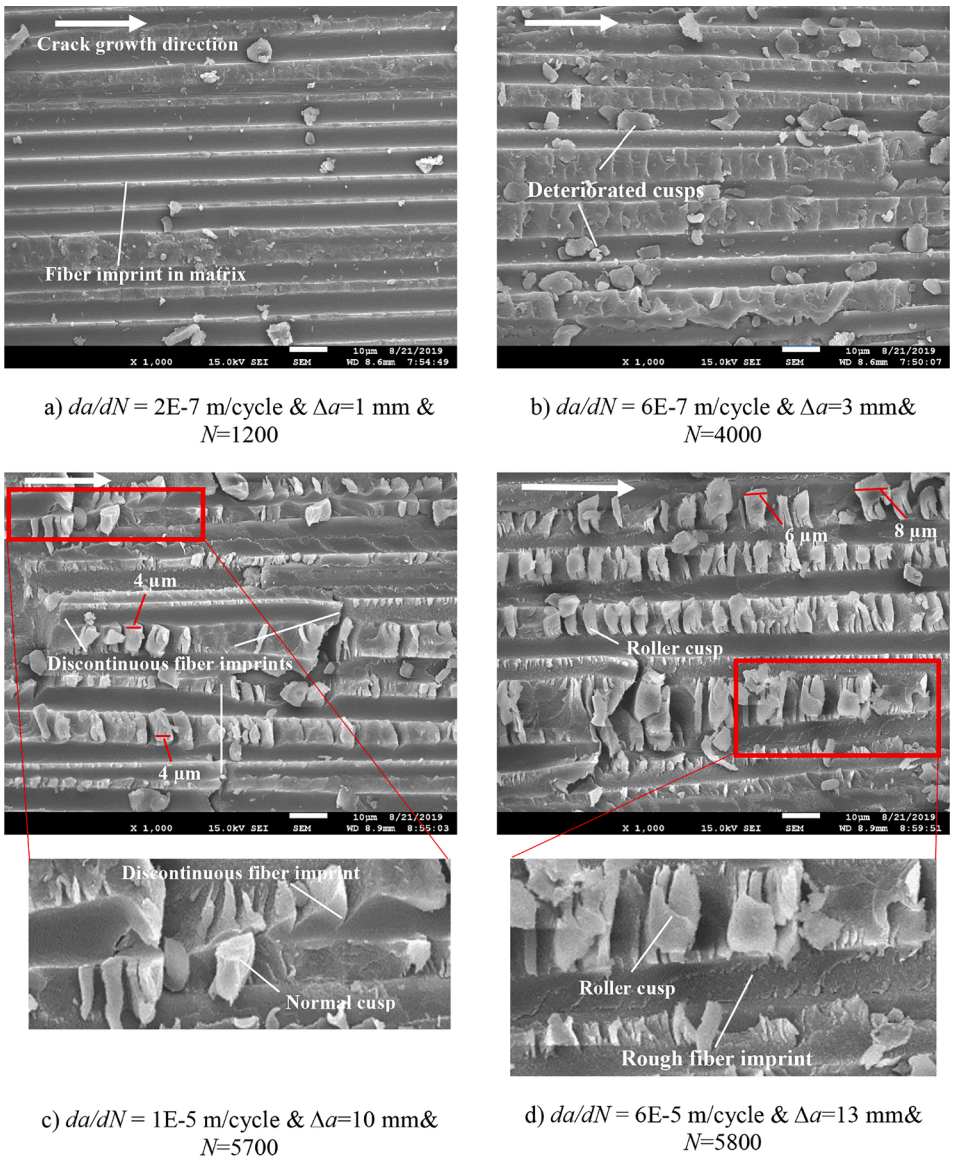

a) da/dN = 2E-7 m/cycle & Δa=1 mm & N=1200

b) da/dN = 6E-7 m/cycle & Δa=3 mm& N=4000

c) da/dN = 1E-5 m/cycle & Δa=10 mm& N=5700

d) da/dN = 6E-5 m/cycle & Δa=13 mm& N=5800

Fig. 8. The fracture surface of the fatigue test specimen (S7-lower surface).

However, because of this increase of the crack growth rate, some shallow traces of the matrix can be found on the fiber, and the fiber imprints surface becomes rougher at higher fatigue delamination growth rates. While, the fiber and fiber imprints surfaces are clean and smooth at the low fatigue crack growth rates. As depicted in Fig. 8d, the cusps are rounded and deformed as rollers for the crack growth rate of da/dN = 6E–5 m/cycle. This is due to the fact that the cusps are infinitesimally deformed in each loading cycle because of the relative slippage of the upper and lower crack surfaces and after many cycles, these infinitesimal deformations are accumulated and the rollers are formed. The axis of these roller cusps is usually perpendicular to the fiber direction.

As depicted in Fig. 8a–d, the surface roughness and the number of damage features increase by enhancing the crack growth rate. In order to quantify the effect of the crack growth rate on the damage features, the potential energy release rate (dU/dN) for the different crack growth rates is calculated. The cyclic potential energy for the load-control fatigue test is calculated using Eq. (11) and it is schematically illustrated in Fig. 9.

$$U_i = \frac{1}{2}(P_{max} + P_{min})(\delta_{max} - \delta_{min})_i \tag{11}$$

where U_i is the potential energy at i^{th} cycle, P_{max} is the maximum load, P_{min} is the minimum load, and δ_{max} and δ_{min} are displacement values which are corresponded to P_{max} and P_{min} at i^{th} cycle, respectively. As seen in Fig. 9, because the maximum and minimum loads are constant in load–control fatigue test, the maximum and minimum displacements and also the crack growth rate (da/dN)

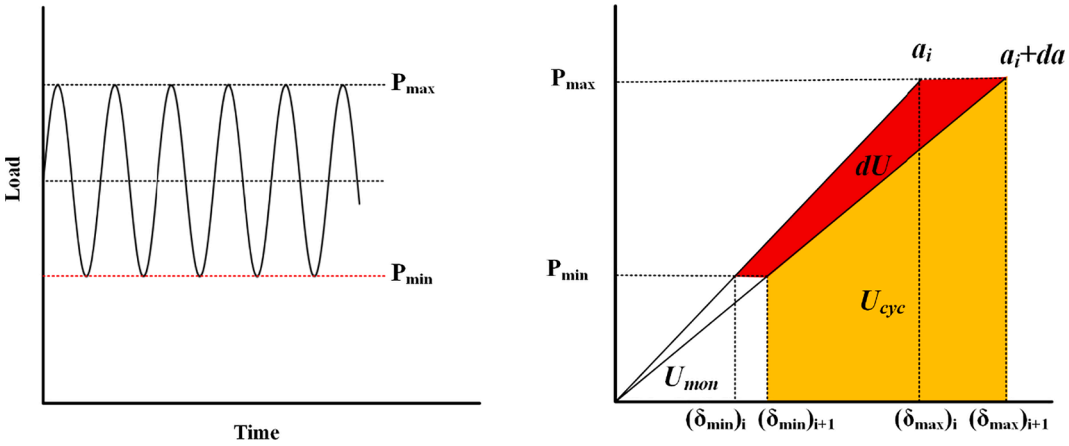

Fig. 9. Changing the potential energy due to an infinitesimal crack growth under load-control fatigue test (a_i is the crack length at i^{th} cycle and da is the infinitesimal crack growth in one cycle).

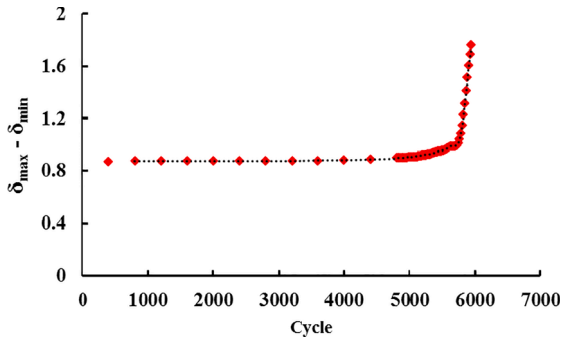

Fig. 10. The increase of the displacement range per cycle for specimen S7.

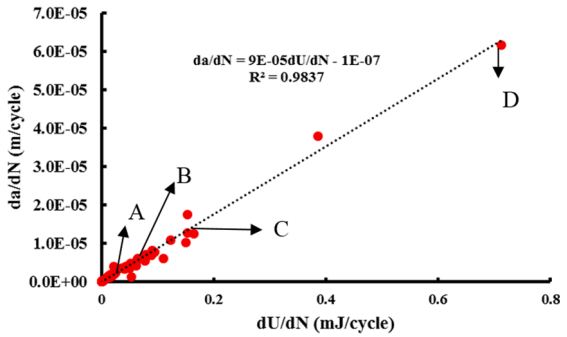

Fig. 11. The relationship of the potential energy dissipation and the fatigue crack growth rate for specimen S7.

continuously increase while the crack propagates during the fatigue test. In addition, as shown in Fig. 10, the term of ($\delta_{max} - \delta_{min}$) increases by the crack propagation. Consequently, according to Eq. (11), the cyclic potential energy increases by enhancing the crack growth rate. Therefore, the rougher surface and more damages observed in Fig. 8c and d are corresponded to the high potential energy release rate.

The potential energy release rate or the rate of energy dissipation, dU/dN, is calculated using Eq. (12):

$$\frac{dU}{dN} = \frac{U_{i+1} - U_i}{N_{i+1} - N_i} \tag{12}$$

where U_{i+1} and U_i are the corresponding potential energies to cycles $i + 1$ and i, and N_{i+1} and N_i are $i + 1^{th}$ and i^{th} cycles, respectively.

Fig. 11 shows the crack growth rate, da/dN, plotted against the potential energy release rate, dU/dN, for specimen S7. As it is

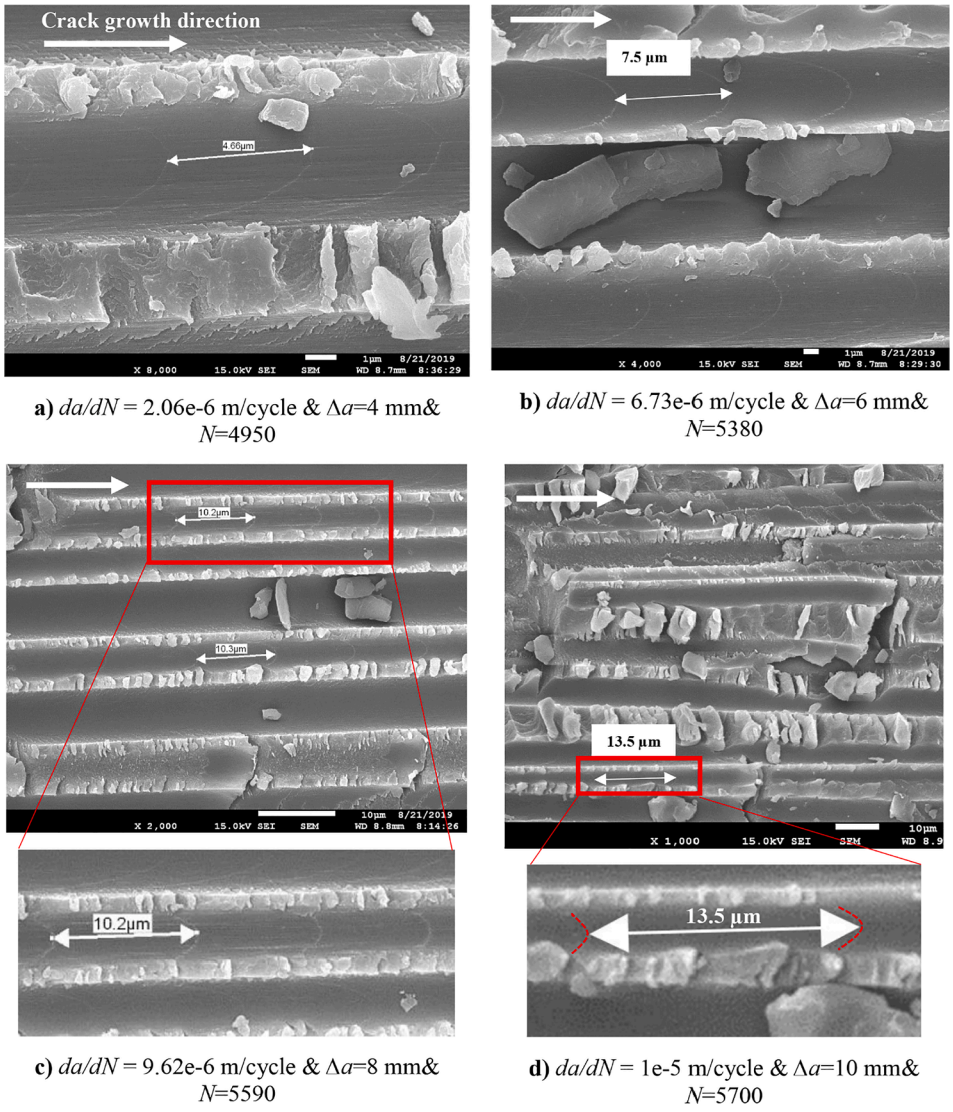

a) da/dN = 2.06e-6 m/cycle & Δa=4 mm& N=4950

b) da/dN = 6.73e-6 m/cycle & Δa=6 mm& N=5380

c) da/dN = 9.62e-6 m/cycle & Δa=8 mm& N=5590

d) da/dN = 1e-5 m/cycle & Δa=10 mm& N=5700

Fig. 12. The striation marks on fatigue surface of S7 specimen.

obvious in Fig. 11, there is a linear relationship between dU/dN and da/dN. The corresponding points of the curve to the images depicted in Fig. 8a–d are marked by letters of A, B, C, and D in Fig. 11. By comparing Figs. 8 and 11, it is found that the damage features completely depend on the dissipated potential energy per cycle, dU/dN. It means that more damage features (see Fig. 8d) indicate more energy dissipation (see Fig. 11-point D).

The other interesting damage feature on the fatigue fracture surface, which is usually visible in high-magnified SEM images, is striation lines (see Fig. 12). As mentioned before, striations are marks created on the fatigue surface which show the incremental growth of the fatigue crack. Striation lines show the crack tip position at the time it was made. The striation indications are made due to the fracture of the molecular chains at the tip of the crack following limited stretching [41]. As seen in Fig. 12, striations are typically curvy as parabolic shapes that show the direction of the global crack growth. It is reported that each striation occurs as a result of a single loading cycle [52]. According to this hypothesis, the striations space indicates the crack growth rate at each cycle. For example, according to Fig. 12a, when the crack propagated 4 mm (Δa = 4 mm) the striations space was 4.66 μm which shows the crack growth rate at this point, da/dN, is 4.66 μm/cycle. By comparing Fig. 12a–d, it is found that by increasing the crack growth rate, da/dN, the striations space increases.

It is worth mentioning that the striation patterns are not visible at the beginning of the crack growth (when Δa < 3 mm). It is because in this region the crack growth rate is very slow and the striation lines is not large enough to be visible in SEM images. In addition, at very high crack growth rates, the fiber imprints become rough and discontinuous which completely mask the striation lines.

According to Fig. 13, there is a linear relationship between striations space and strain energy release rate range (ΔG_S). ΔG_S is the

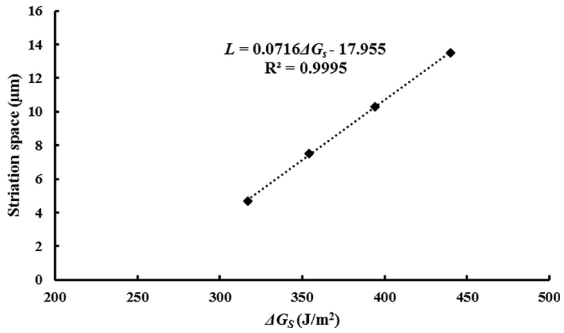

Fig. 13. The relationship of striations space between driving force (ΔG_S).

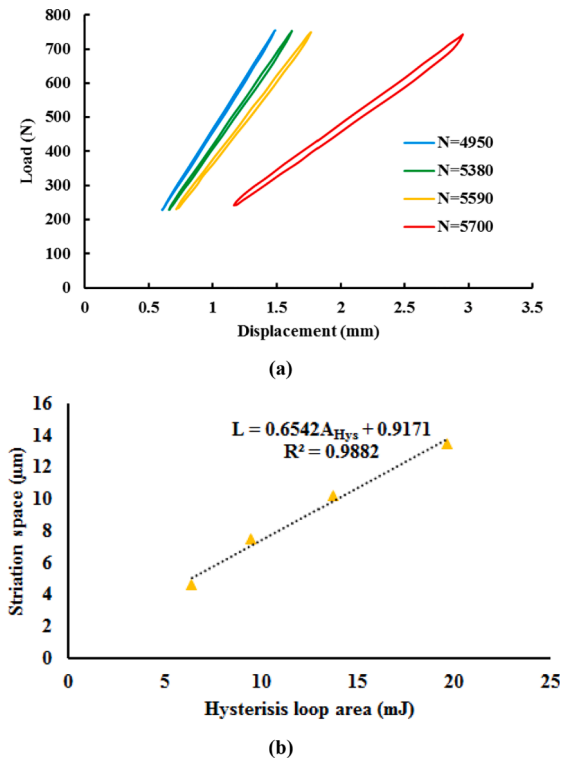

Fig. 14. (a) The hysteresis loops and (b) the relationship between the hysteresis loop area and the striations space.

driving force of the crack propagation calculated from Eq. (10). It is noteworthy that this relationship is only valid for 315 J/m^2 $< \Delta G_S <$ 440 J/m^2.

The loading–unloading curves for the 4 different cycle numbers are illustrated in Fig. 14a. By comparing the curves, it is revealed that by increasing the cycle numbers and accumulation of the damage, the slope of the curves decreases, which represents the stiffness degradation, while the area inside the load-unloading loop increases. The area of the closed hysteresis loop can be related to the energy dissipation mechanisms, such as friction between the upper and lower crack surfaces, friction between the specimen and the roller supports, and also the damage growth [53]. The area of the hysteresis loops versus their corresponding striation space is shown in Fig. 14b. As can be seen, a line can be fitted to the data points which shows when damage propagates and the dissipated energy increases, the striation length increases.

3.4. Acoustic emission study

Fig. 15 shows the amplitude of the originated AE events during 11 cycles of the mode-II fatigue test as a representative of the fatigue test. As observed, the AE events occurred in both loading and unloading phases in each cycle.

A portion of the dissipated energy in each cycle is dedicated to the crack growth and the rest is harvested to induce heat in the

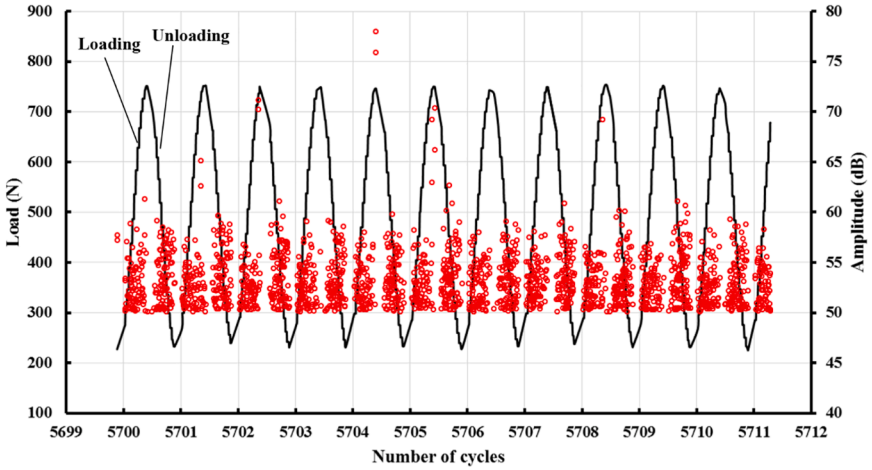

Fig. 15. The 11 cycles of the mode-II fatigue test and the amplitude of the originated AE events for specimen S7 (the cycles were selected around point C in Fig. 11).

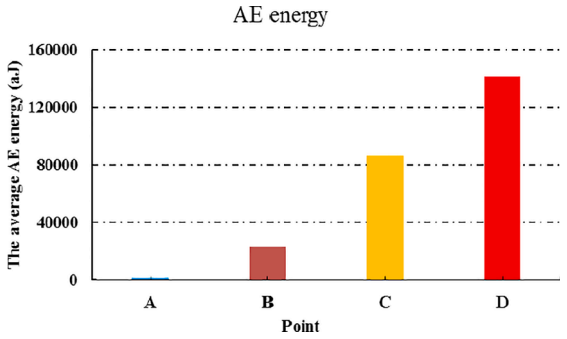

Fig. 16. The average AE energy for each point of fracture surface corresponding Fig. 8.

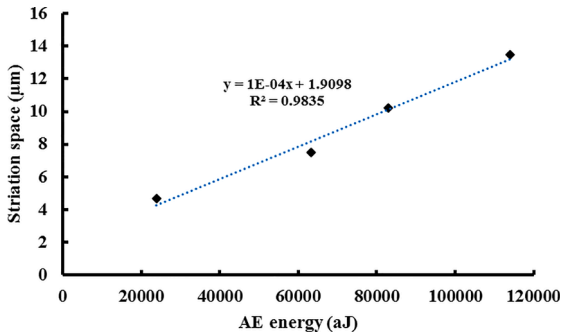

Fig. 17. The striation space vs AE energy.

damage zone ahead of the crack tip. The AE energy generated by the crack growth can be used for characterization of the formed cusps. To this aim, energy values of the corresponding AE signals in points A, B, C, and D, depicted in Fig. 8, are extracted. Because finding the exact cycle number associated with these points is not possible, the average AE energy of the AE events occurred during five cycles before and after the desired cycle number is considered as the representative AE energy of that point. By comparing Figs. 16–18, it is found that as much as the fracture surface became rougher and the cusps enlarged, the released AE energy due to the induced damages increased.

As aforementioned, the striation marks show the amount of the crack growth in one cycle, so it is anticipated that those marks were associated to the AE energy generated by the infinitesimal crack growth in that cycle. In order to show this relationship experimentally, the corresponding cycle numbers to the images depicted in Fig. 12a–d are obtained and the released AE energy in those cycles is plotted

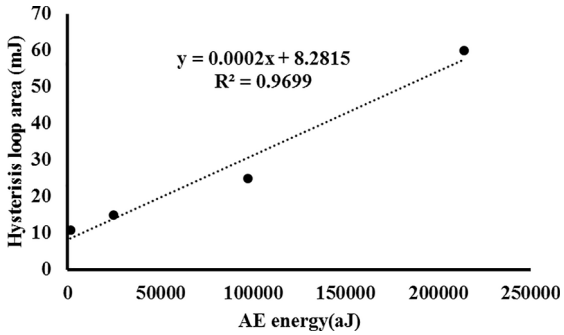

Fig. 18. The relationship between AE energy and hysteresis loop area.

versus the size of the associated striations space (see Fig. 17). As it is obvious in Fig. 17, there is a linear relationship between these two parameters. In addition, the AE energy versus the area of the closed hysteresis loops is shown in Fig. 18, which a linear relationship between the dissipated energy and the generated AE signals can be established.

4. Conclusion

The aim of the present study was to quantify mode-II fatigue damage features such as cusp and striation patterns by means of the SEM and AE techniques. For this purpose, the specimens were prepared and subjected to the quasi-static and fatigue mode II loading conditions according to ASTM D7905M standard. The fracture surface of the specimens was then investigated using SEM images and the damage features, such as fiber imprint, cusps, roller cusps, and striations, were identified. To quantify the effect of the fatigue crack growth rate, da/dN, on the damage features, the potential energy release rate (dU/dN) for the different crack growth rates was calculated. It was found that more damage features indicate more dissipated energy. In addition, there was a linear relationship between the fatigue striation space with the strain energy release rate range (ΔGs) and the hysteresis loop area. Finally, the AE technique was used to characterize the damage features and it was shown that higher AE energy indicates larger cusps and striation spaces.

Declaration of Competing Interest

The authors declare that they have no known competing financial interests or personal relationships that could have appeared to influence the work reported in this paper.

References

[1] Taheri H, Oliaei M, Ipakchi H, Saghafi H. Toughening phenolic composite laminates by interleaving hybrid pyrolytic carbon/polyvinyl butyral nanomat. Compos B Eng 2020;191:107981.
[2] Mohammadi R, Najafabadi MA, Saghafi H, Zarouchas D. Fracture and fatigue behavior of carbon/epoxy laminates modified by nanofibers. Compos A Appl Sci Manuf 2020;137:106015.
[3] Daneshjoo Z, Shokrieh MM, Fakoor M, Alderliesten R, Zarouchas D. Physics of delamination onset in unidirectional composite laminates under mixed-mode I/II loading. Eng Fract Mech 2019;211:82–98.
[4] Saeedifar M, Mansvelder J, Mohammadi R, Zarouchas D. Using passive and active acoustic methods for impact damage assessment of composite structures. Compos Struct 2019;226:111252.
[5] Brugo T, Minak G, Zucchelli A, Yan XT, Belcari J, Saghafi H, et al. Study on Mode I fatigue behaviour of Nylon 6,6 nanoreinforced CFRP laminates. Compos Struct 2017;164:51–7.
[6] Moallemzadeh AR, Sabet SAR, Abedini H, Saghafi H. Investigation into high velocity impact response of pre-loaded hybrid nanocomposite structure. Thin-Walled Struct 2019;142:405–13.
[7] Li X, Kupski J, Teixeira De Freitas S, Benedictus R, Zarouchas D. Unfolding the early fatigue damage process for CFRP cross-ply laminates. Int J Fatigue 2020;140.
[8] Mohammadi R, Najafabadi MA, Saghafi H, Zarouchas D. Mode-II fatigue response of AS4/8552 carbon/epoxy composite laminates interleaved by electrospun nanofibers. Thin-Walled Struct 2020;154:106811.
[9] Ekhtiyari A, Shokrieh MM, Alderliesten R. Loading rate effects on mode-I delamination in glass/epoxy and glass/CNF/epoxy laminated composites. Eng Fract Mech 2020;228:106908.
[10] Saeedifar M, Ahmadi Najafabadi M, Mohammadi K, Fotouhi M, Hosseini Toudeshky H, Mohammadi R. Acoustic emission-based methodology to evaluate delamination crack growth under quasi-static and fatigue loading conditions. J Nondestr Eval 2017;37:1.
[11] Mohammadi R, Saeedifar M, Toudeshky HH, Najafabadi MA, Fotouhi M. Prediction of delamination growth in carbon/epoxy composites using a novel acoustic emission-based approach. J Reinf Plast Compos 2015;34:868–78.
[12] Saeedifar M, Fotouhi M, Najafabadi MA, Toudeshky HH. Interlaminar fracture toughness evaluation in glass/epoxy composites using acoustic emission and finite element methods. J Mater Eng Perform 2015;24:373–84.
[13] Garcia Perez P, Bouvet C, Chettah A, Dau F, Ballere L, Pérès P. Effect of unstable crack growth on mode II interlaminar fracture toughness of a thermoplastic PEEK composite. Eng Fract Mech 2019;205:486–97.
[14] Greenhalgh E. Failure analysis and fractography of polymer composites. Elsevier; 2009.
[15] Rubiera S, Argüelles A, Viña J, Rocandio C. Study of the phenomenon of fatigue delamination in a carbon-epoxy composite under mixed mode I/II fracture employing an asymmetric specimen. Int J Fatigue 2018;114:74–80.
[16] Yao L, Sun Y, Guo L, Lyu X, Zhao M, Jia L, et al. Mode I fatigue delamination growth with fibre bridging in multidirectional composite laminates. Eng Fract Mech 2018;189:221–31.

[17] Gilchrist MD, Svensson N. A fractographic analysis of delamination within multidirectional carbon/epoxy laminates. Compos Sci Technol 1995;55:195–207.
[18] Jollivet T, Greenhalgh E. Fractography, a powerful tool for identifying and understanding fatigue in composite materials. Procedia Eng 2015;133:171–8.
[19] Amaral L. Towards fundamental understanding of interlaminar ply delamination growth under mode II and mixed-mode loading. Delft University of Technology; 2018.
[20] Khan R, Alderliesten R, Badshah S, Benedictus R. Effect of stress ratio or mean stress on fatigue delamination growth in composites: Critical review. Compos Struct 2015;124:214–27.
[21] Amaral L, Zarouchas D, Alderliesten R, Benedictus R. Energy dissipation in mode II fatigue crack growth. Eng Fract Mech 2017;173:41–54.
[22] Vedrtnam A. Novel treatment methods for improving fatigue behavior of laminated glass. Compos B Eng 2019;167:180–98.
[23] Kaushik V, Ghosh A. Experimental and numerical investigation of Mode-I & Mode-II fatigue crack growth in unidirectional composites using XIGA-CZM approach. Int J Fatigue 2020;134:105461.
[24] Amaral L, Alderliesten R, Benedictus R. Understanding mixed-mode cyclic fatigue delamination growth in unidirectional composites: An experimental approach. Eng Fract Mech 2017;180:161–78.
[25] Srivatsan TA. Review of: Fractography: Observing, measuring, and interpreting fracture surface topography, D. Hull. Mater Manuf Process 2009;24:1229–30.
[26] Hiley MJ. Fractographic study of static and fatigue failures in polymer composites. Plast Rubber Compos 1999;28:210–27.
[27] Khan R, Alderliesten R, Benedictus R. Two-parameter model for delamination growth under mode I fatigue loading (Part A: Experimental study). Compos A Appl Sci Manuf 2014;65:192–200.
[28] Khan R, Alderliesten R, Benedictus R. Two-parameter model for delamination growth under mode I fatigue loading (Part B: Model development). Compos A Appl Sci Manuf 2014;65:201–10.
[29] Saeedifar M, Najafabadi MA, Zarouchas D, Toudeshky HH, Jalalvand M. Barely visible impact damage assessment in laminated composites using acoustic emission. Compos B Eng 2018;152:180–92.
[30] Mohammadi R, Najafabadi MA, Saeedifar M, Yousefi J, Minak G. Correlation of acoustic emission with finite element predicted damages in open-hole tensile laminated composites. Compos B Eng 2017;108:427–35.
[31] Barile C, Casavola C, Pappalettera G, Kannan VP. Application of different acoustic emission descriptors in damage assessment of fiber reinforced plastics: A comprehensive review. Eng Fract Mech 2020:107083.
[32] Saeedifar M, Najafabadi MA, Zarouchas D, Toudeshky HH, Jalalvand M. Clustering of interlaminar and intralaminar damages in laminated composites under indentation loading using Acoustic Emission. Compos B Eng 2018;144:206–19.
[33] Saeedifar M, Zarouchas D. Damage characterization of laminated composites using acoustic emission: A review. Compos Part B: Eng 2020:108039.
[34] Mouzakis DE, Dimogianopoulos DG. Acoustic emission detection of damage induced by simulated environmental conditioning in carbon fiber reinforced composites. Eng Fract Mech 2019;210:422–8.
[35] Fotouhi M, Suwarta P, Jalalvand M, Czel G, Wisnom MR. Detection of fibre fracture and ply fragmentation in thin-ply UD carbon/glass hybrid laminates using acoustic emission. Compos A Appl Sci Manuf 2016;86:66–76.
[36] Barile C, Casavola C, Pappalettera G, Vimalathithan PK. Damage characterization in composite materials using acoustic emission signal-based and parameter-based data. Compos B Eng 2019;178:107469.
[37] Ben Ameur M, El Mahi A, Rebiere J-L, Gimenez I, Beyaoui M, Abdennadher M, et al. Investigation and identification of damage mechanisms of unidirectional carbon/flax hybrid composites using acoustic emission. Eng Fract Mech 2019;216:106511.
[38] Malpot A, Touchard F, Bergamo S. An investigation of the influence of moisture on fatigue damage mechanisms in a woven glass-fibre-reinforced PA66 composite using acoustic emission and infrared thermography. Compos B Eng 2017;130:11–20.
[39] Jeannin T, Gabrion X, Ramasso E, Placet V. About the fatigue endurance of unidirectional flax-epoxy composite laminates. Compos B Eng 2019;165:690–701.
[40] Maleki A, Saeedifar M, Ahmadi Najafabadi M, Zarouchas D. The fatigue failure study of repaired aluminum plates by composite patches using Acoustic Emission. Eng Fract Mech 2019;210:300–11.
[41] HexPly® 8552 Epoxy matrix (180°C/356°F curing matrix) in FTA 072e. Hexcel Composites Publication; 2013.
[42] Standard A. D7905/D7905M-14. Standard test method for determination of the mode II interlaminar fracture toughness of unidirectional fiber-reinforced polymer matrix composites; 2014.
[43] ASTM E976-10. Standard guide for determining the reproducibility of acoustic emission sensor response. West Conshohocken (PA): ASTM International; 2010.
[44] Ferdous W, Manalo A, Peauril J, Salih C, Raghava Reddy K, Yu P, et al. Testing and modelling the fatigue behaviour of GFRP composites – Effect of stress level, stress concentration and frequency. Eng Sci Technol, Int J 2020;23:1223–32.
[45] Liang S, Gning P-B, Guillaumat L. Properties evolution of flax/epoxy composites under fatigue loading. Int J Fatigue 2014;63:36–45.
[46] Vieira PR, Carvalho EML, Vieira JD, Toledo Filho RD. Experimental fatigue behavior of pultruded glass fibre reinforced polymer composite materials. Compos B Eng 2018;146:69–75.
[47] Wu Z, Wang X, Iwashita K, Sasaki T, Hamaguchi Y. Tensile fatigue behaviour of FRP and hybrid FRP sheets. Compos B Eng 2010;41:396–402.
[48] ASTM E647-15e1. Standard test method for measurement of fatigue crack growth rates. West Conshohocken (PA): ASTM International; 2015. www.astm.org.
[49] Rans C, Alderliesten R, Benedictus R. Misinterpreting the results: How similitude can improve our understanding of fatigue delamination growth. Compos Sci Technol 2011;71:230–8.
[50] Shivakumar KN, Panduranga R, Skujins J, Miller S. Assessment of mode-II fracture tests for unidirectional fiber reinforced composite laminates. J Reinf Plast Compos 2015;34:1905–25.
[51] Zabala H, Aretxabaleta L, Castillo G, Aurrekoetxea J. Loading rate dependency on mode I interlaminar fracture toughness of unidirectional and woven carbon fibre epoxy composites. Compos Struct 2015;121:75–82.
[52] McEvily A, Matsunaga H. On fatigue striations; 2010.
[53] Van Paepegem W, Geyter K, Vanhooymissen P, Degrieck J. Effect of friction on the hysteresis loops from three-point bending fatigue tests of fibre-reinforced composites. Compos Struct 2006;72:212–7.